Check for updates

ADVANCED FUNCTIONAL MATERIALS
www.afm-journal.de

Ultrathin ZIF-8 Coating-Reinforced Enzyme Nanoformulation Avoids Lysosomal Degradation for Senile Osteoporosis Therapy

Shiyuan Liang, Liyuan Chen, Cong Liu, Bowen Guo, Yijie Fan, Zhou Li, Yan Liu,* and Dan Luo**

Antioxidant enzymes are considered to be the most direct and safe candidates to effectively resist oxidative stress and treat senile osteoporosis. However, due to their size, existing enzyme delivery carriers are inevitably endocytosed by cells and subsequently enter endosomes/lysosomes with low pH and rich in acid hydrolase, resulting in the limited therapeutic effects. In this work, an ultrasmall superoxide dismutase (SOD) nanoformulation reinforced with ultrathin ZIF-8 coating (utZIF-SOD) via in situ coordination-mediated self-assembly strategy is constructed. Notably, utZIF-SOD achieves direct, efficient cellular uptake mediated by small size effect, thereby avoiding lysosomal degradation. In particular, ultrathin ZIF-8 coating strengthened the stability of enzyme. Even in aged cells with high oxidative stress levels, utZIF-SOD maintained excellent stability, and its efficiency in scavenging excess intracellular reactive oxygen species (ROS) is ≈1.5 times that of native SOD, better promoting the osteogenic differentiation of aged bone marrow mesenchymal stem cells. In a senile osteoporosis mouse model, the bone mineral density increment after treatment with utZIF-SOD is ≈2 times that of native SOD, achieving the reversal of senile osteoporosis. This work demonstrates the great promise in the synthesis of ultrasmall nanoformulations with ultrathin metal-organic framework coating and opens new avenues for efficient enzyme delivery.

1. Introduction

With the aging of the world population, senile osteoporosis (SOP) has become a worldwide aged-related disease with features of bone loss and destruction of bone microstructure, substantially increasing the health-care costs and life-threatening risks in the elderly.[1,2] At present, it is well accepted that excessive reactive oxygen species (ROS), as a result of oxidative stress with the imbalance between oxidation and antioxidation in the aging process, are the main cause of SOP.[3,4] In particular, antioxidant enzymes are considered to be the most direct and safe candidates to effectively resist oxidative stress and treat SOP in the elderly.[5] As an important antioxidant enzyme in biological systems, superoxide dismutase (SOD) can effectively eliminate ROS, which has been widely used in the therapeutics of oxidative stress-mediated pathophysiological diseases, such as osteoarthritis, inflammatory bowel disease and ischemia-reperfusion injury.[6–10]

Currently, native enzymes have exhibited the outstanding characteristics of high specificity, effectiveness, and low toxicity in treating diseases,[11–13] but their therapeutic effects are greatly limited due to low membrane permeability, short circulating half-life in the delivery process, and particularly poor stability in aged cells with high oxidative stress levels.[11,14–17] To cope with these challenges and limitations, researchers have integrated proteins with nanocarriers to promote cellular uptake and increase their stability.[18] Among numerous carriers reported so far, metal-organic frameworks (MOFs) have been widely used as drug delivery carriers in recent years due to flexible structure,[19–21] tunable pore size,[22,23] easy functionalization,[24,25] and mild synthesis conditions.[26,27] Zeolite imidazolate framework-8 (ZIF-8) is considered as an ideal carrier for enzyme immobilization because of its easy synthesis, excellent chemical and thermal stability and negligible cytotoxicity.[28] As a carrier, it has been widely used in biomedical fields, such as antibacterial, anti-inflammatory, tissue repair, tumor treatment, etc.[22] Especially in the treatment of osteoporosis, Zn^{2+} contained in ZIF-8 also has anti-inflammatory and osteogenic effects, which is more beneficial to the recovery of osteoporosis.[29] However, due to size effects, existing enzyme delivery carriers are inevitably endocytosed by

S. Liang, C. Liu, B. Guo, Y. Fan, Z. Li, D. Luo
Beijing Institute of Nanoenergy and Nanosystems
Chinese Academy of Sciences
Beijing 101400, China
E-mail: zli@binn.cas.cn; luodan@binn.cas.cn

S. Liang, L. Chen, Y. Liu
Central Laboratory
Department of Orthodontics
Peking University School and Hospital for Stomatology & National Center for Stomatology & National Clinical Research Center for Oral Diseases & National Engineering Research Center of Oral Biomaterials and Digital Medical Devices & Beijing Key Laboratory of Digital Stomatology & Research Center of Engineering and Technology for Computerized Dentistry Ministry of Health & NMPA Key Laboratory for Dental Materials & National Engineering Research Center of Oral Biomaterials and Digital Medical Devices
Beijing 100081, China
E-mail: orthoyan@bjmu.edu.cn

S. Liang, C. Liu, Y. Fan, Z. Li, D. Luo
School of Nanoscience and Engineering
University of Chinese Academy of Sciences
Beijing 100049, China

The ORCID identification number(s) for the author(s) of this article can be found under https://doi.org/10.1002/adfm.202410931

DOI: 10.1002/adfm.202410931

 © 2024 Wiley-VCH GmbH

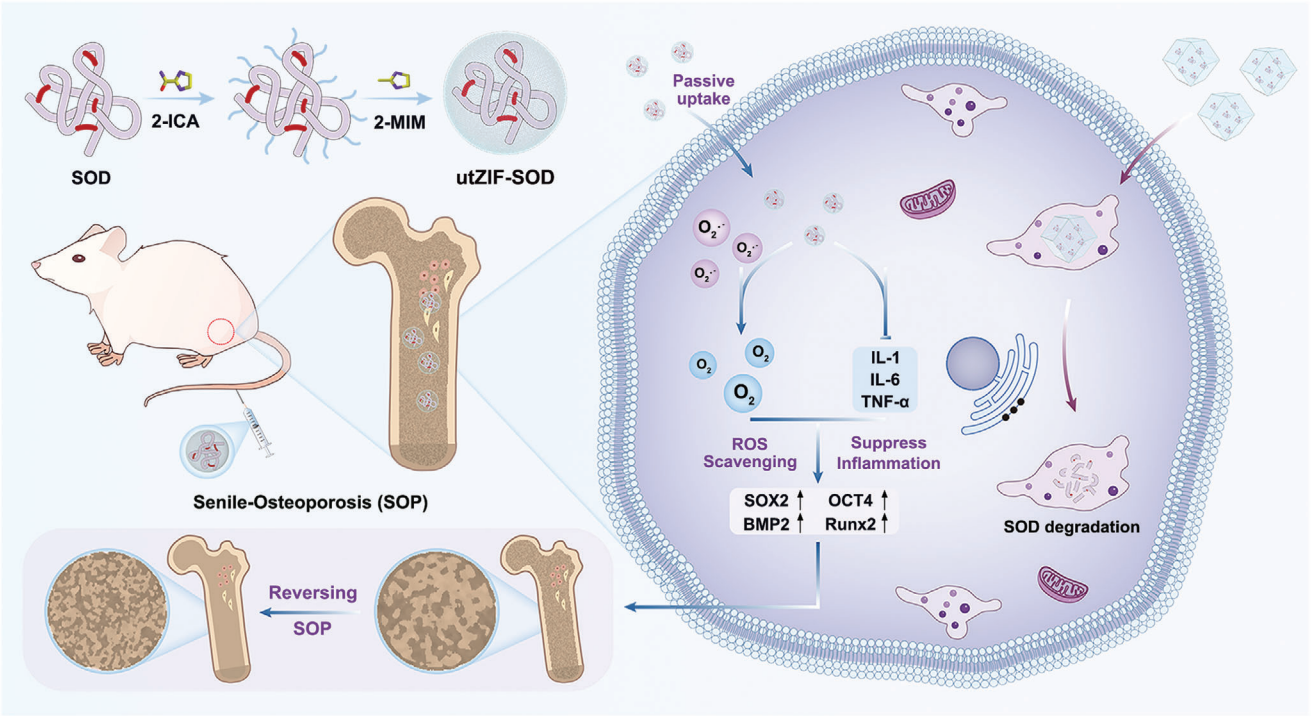

Figure 1. Schematic diagram of utZIF-SOD treating senile osteoporosis mice. utZIF-SOD achieved direct and efficient cellular uptake mediated by small size effect, rather than being endocytosed. utZIF-SOD could effectively scavenge excess intracellular ROS, thereby reversing senile osteoporosis.

cells and then enter endosomes/lysosomes via various endocytosis pathways, including reticulin and caveolin-mediated, reticulin and caveolin-independent pathways, macropinocytosis, and phagocytosis.[30,31] Certainly, plenty of methods have been developed to enable protein@MOF nanoparticles to escape from lysosomes effectively,[32,33] but a certain amount of enzyme nanoformulation is still confined to endosomes/lysosomes with low pH and rich in acid hydrolase, resulting in the inhibition of enzyme activity and limited therapeutic effects. It is worth mentioning that, smaller nanoparticles (< 10 nm) can enter the cell via direct membrane penetration, avoiding entry into lysosomes and subsequent degradation, thus allowing more nanoparticles to be utilized for subsequent treatment.[31] Hence, ultrasmall enzyme nanoformulation is a rational designing strategy, enabling enzymes to directly penetrate into cells via passive uptake, thereby maintaining excellent stability and catalytic activity in aged cells with high oxidative stress levels.

In this study, encapsulation SOD with ZIF-8 via in situ coordination-mediated self-assembly strategy was employed to prepare an ultrasmall SOD nanoformulation reinforced with ultrathin ZIF-8 coating (utZIF-SOD), which effectively reduced oxidative stress for treating SOP (**Figure 1**). Owing to its ultrasmall size, utZIF-SOD could be absorbed and utilized by cells through direct, efficient cellular uptake rather than being endocytosed, thereby evading lysosomal degradation and exhibiting high utilization efficiency. In particular, the ultrathin ZIF-8 coating strengthened the stability of the enzyme. Even in aged cells with high oxidative stress levels, utZIF-SOD could still effectively eliminate excess ROS, reducing the aged-related phenotype of bone marrow mesenchymal stem cells (BMSCs), thereby leading to enhanced proliferation, migration, and osteogenesis ability. As a result, utZIF-SOD prepared by in situ coordination-mediated self-assembly strategy would prevent bone loss in adult mice, accelerate bone regeneration in aged rodents, and ultimately reverse SOP.

2. Result and Discussion

2.1. Synthesis and Characterization of utZIF-SOD

The synthesis process of utZIF-SOD via in situ coordination-mediated self-assembly strategy was as follows (**Figure 2a**). First, the free amino group (-NH_2) of the protein was chemically coupled with the carboxyl group (-COOH) in 2-Imidazolecarboxylic Acid (2-ICA), resulting in the growth of a layer of organic ligand on the protein's surface in situ. Then, the organic ligand 2-Methylimidazole (2-MIM) was added and thoroughly mixed. Finally, the added metal ion Zn^{2+} was assembled with the imidazole ring in the 2-ICA and 2-MIM via in situ coordination-mediated self-assembly, generating utZIF-SOD. Transmission electron microscopy (TEM) was used to characterize the resulting utZIF-SOD. The utZIF-SOD exhibited spherical morphology with an average particle size of 8.8 ± 0.9 nm (Figure 2b). Representative atomic force microscope (AFM) images of utZIF-SOD revealed an average size of approximately 9.7 ± 1.5 nm (Figure 2c), consistent with the TEM result. The average size of pure SOD measured by AFM was ≈7.2 nm (Figure S1, Supporting Information), indicating successful encapsulation of SOD with ZIF-8, with a shell thickness of ≈1.25 nm (Figure 2d). To further validate the structure of utZIF-SOD, dynamic light scattering (DLS) (Figure 2e)

© 2024 Wiley-VCH GmbH

16163028, 0, Downloaded from https://onlinelibrary.wiley.com/doi/10.1002/adfm.202410931 by Cas-Beijing Institution Of, Wiley Online Library on [05/09/2024]. See the Terms and Conditions (https://onlinelibrary.wiley.com/terms-and-conditions) on Wiley Online Library for rules of use; OA articles are governed by the applicable Creative Commons License

16163028, 0, Downloaded from https://onlinelibrary.wiley.com/doi/10.1002/adfm.202410931 by Cas-Beijing Institution Of, Wiley Online Library on [05/09/2024]. See the Terms and Conditions (https://onlinelibrary.wiley.com/terms-and-conditions) on Wiley Online Library for rules of use; OA articles are governed by the applicable Creative Commons License

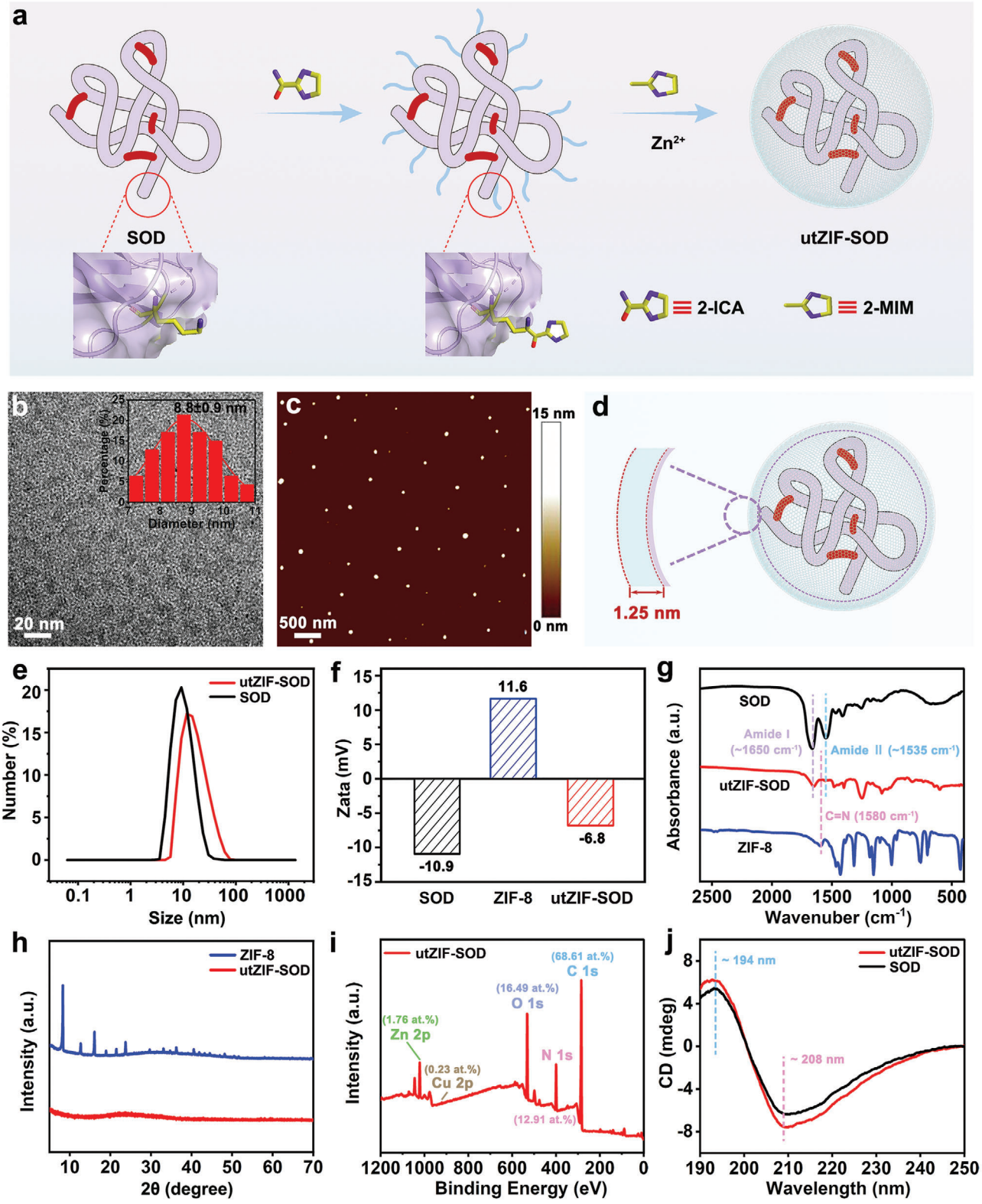

Figure 2. Synthesis and characterization of utZIF-SOD. a) Schematic illustration of in situ growth synthesis of utZIF-SOD. b) A representative TEM image and grain diameter distribution map of utZIF-SOD. c) A representative AFM image of utZIF-SOD. d) Schematic diagram of shell thickness of utZIF-SOD. e) DLS measurements revealing the size distribution of native SOD and utZIF-SOD. f) Zeta potentials of native SOD and utZIF-SOD. g) FTIR spectra of native SOD, utZIF-SOD and ZIF-8. h) XRD patterns of utZIF-SOD and ZIF-8. i) XPS spectra of utZIF-SOD. j) CD spectra of native SOD and utZIF-SOD.

© 2024 Wiley-VCH GmbH

was employed to measure the particle size distribution and zeta potential of native SOD and utZIF-SOD (Figure 2f). Native SOD exhibited a negative charge (−10.9 mV) with its size distribution concentrated at 9.2 nm. In comparison, utZIF-SOD displayed a slightly negative charge (−6.8 mV), with its size distribution concentrated at 11.6 nm, indicating successful encapsulation of SOD with ZIF-8 shell.

Successful encapsulation was further validated by Fourier-transform infrared (FTIR) spectra (Figure 2g). UtZIF-SOD exhibited characteristic absorption peaks of SOD at ≈1650 cm^{-1} and ≈1535 cm^{-1}, attributed to the amide I and II bands, respectively.[18,34] The characteristic absorption peak of the C═N bond in the imidazole ring was observed near the position of ≈1580 cm^{-1}, corresponding to the ZIF-8 shell of utZIF-SOD.[33] In the subsequent powder X-ray diffraction (XRD) characterization, utZIF-SOD did not exhibit the obvious crystal form as ZIF-8 nanoparticles (Figure 2h), possibly due to the defects in the ultrathin ZIF-8 shell with poor crystallinity. The surface composition of the as-prepared samples was investigated by X-ray photoelectron spectroscopy (XPS). As shown in the survey scanning XPS spectra (Figure 2i), all peaks were attributed to C (68.61 at.%), N (12.91 at.%), O (16.49 at.%), Zn (1.76 at.%), Cu (0.23 at.%), respectively. In the C 1s spectrum (Figure S2a, Supporting Information), the peaks at 284.8 eV, 285.6 eV, 286.58 eV, 287.19 eV and 288.34 eV were attributed to C–C, C═N, C–O–C, C–N, O–C═O and C–O, respectively. The peak at 399.3 eV was attributed to C═N, whereas the peaks at 400.8 eV and 406.8 eV were C–N and N–H, respectively (Figure S2b, Supporting Information). The O 1s peaks at 531.6 and 532.6 eV could be regarded as C–O and C═O, respectively (Figure S2c, Supporting Information). Additionally, the Zn 2p spectrum was displayed at 1045.4 eV and 1022.4 eV, which were assigned to Zn $2p_{1/2}$ and Zn $2p_{3/2}$ (Figure S2d, Supporting Information) of Zn^{2+}. Analogously, the Cu 2p spectrum showed two merged characteristic peaks (Cu $2p_{1/2}$ at 953.2 eV, Cu $2p_{3/2}$ at 932.4 eV), which were referred to the Cu^{2+} species (Figure S2e, Supporting Information). Among them, the atomic percentage of Zn was about 7.65 times that of Cu, which further proved that SOD was successfully encapsulated with ZIF-8. In order to investigate whether the structure of SOD changed before and after encapsulation, the structural stability was characterized by circular dichroism (CD) (Figure 2j). The CD peak shape of native SOD in the range of 190–250 nm showed a positive peak near 194 nm and a negative peak in the range of 208 nm, which was a typical CD spectrum with β conformation components as the main component.[36,37] Consistently, the CD peak with native SOD was also observed in utZIF-SOD, and the peak position did not change obviously, which indicated that the structure of native SOD was not affected after the protein was encapsulated with ZIF-8. In order to further confirm the successful encapsulation of SOD by ZIF-8, we replaced Zn^{2+} in the ZIF-8 shell with Ni^{2+} (Ni-utZIF-SOD).[38,39] Scanning transmission electron microscopy (STEM) image (Figure S3, Supporting Information) revealed uniform element distributions of N, O, P, Zn, and Ni in Ni-utZIF-SOD. XPS analysis (Figure S4, Supporting Information) confirmed that Ni effectively replaced Zn in the ZIF-8 shell, with no significant changes observed in the proportion and peak position of other elements. This further verified the successful encapsulation of SOD with the ZIF-8 shell.

2.2. Catalytic Activity and Stability of utZIF-SOD

Catalytic activity and stability of enzymes were the critical issues during delivery in vivo.[40] Particularly, various unamiable environments could affect the structure of proteins,[3] ultimately leading to their denaturation and inactivation (**Figure 3a**). Due to the imbalance of oxidative stress between oxidation and antioxidation, aged cells have higher ROS levels. High ROS levels can easily lead to lipid peroxidation, protein degeneration, DNA damage and oxidative damage of other biomolecules,[41] so we explored the effect of high ROS levels on SOD activity and structure in utZIF-SOD. After native SOD and utZIF-SOD were treated with high concentration of H_2O_2, the $O_2^{\bullet-}$ scavenging ability of native SOD were significantly reduced. However, utZIF-SOD still showed higher ROS scavenging efficiency, demonstrating that utZIF-SOD could maintain excellent stability and catalytic activity in aged cells with high oxidative stress levels (Figure 3b; Figure S5, Supporting Information). In the CD spectra, it was found that the negative absorption peak at 208 nm and the positive absorption peak near 194 nm of native SOD shifted obviously after high concentration of H_2O_2 treatment, while the spectral band of utZIF-SOD remained basically unchanged (Figure 3c). Relevant studies have proved that osteoporosis is a pathological disease associated with oxidative stress disorders characterized by heavy metal ions overload.[42,41] In the lesion location of osteoporosis, metal ions will reduce the activity of enzymes, thus affecting the antioxidant function of aged cells.[43] After treating SOD and utZIF-SOD with different heavy metal ions (Pb and Fe), respectively, the enzyme activity of native SOD was obviously decreased, but the activity of utZIF-SOD was not affected (Figure 3f,h). Different pH conditions will also affect the activity of the enzyme. Because the pH of aged cells is lower than that of normal cells and the pH of mitochondria is about 8, we explored the enzyme activity under the conditions of pH = 6.5 and pH = 8, respectively.[44,45] Compared with normal conditions, SOD activity decreased, while utZIF-SOD activity remained unchanged (Figure S6, Supporting Information). In addition, high temperature can lead to denaturation and inactivation of enzymes.[46] The effect of high temperature on enzyme activity of native SOD and utZIF-SOD were also investigated, and the change trend of enzyme activity was consistent with the effect of high ROS levels and heavy metals (Figure 3d). This superiority could be attributed to the protective effect of the ZIF-8 shell on SOD, which could prevent functional inactivation resulting from structural damage in the unamiable environments. Consistently, significant changes were observed in the negative absorption peak of native SOD within the range of 197–240 nm in the subsequent CD results. Particularly noteworthy was the substantial shift or near disappearance of the positive peak near 194 nm (Figure 3e, g,i). Conversely, the spectral band of utZIF-SOD remained basically unchanged. These results suggested that high ROS levels, elevated temperatures, and heavy metals disrupted secondary structure of native SOD, whereas they showed minimal impact on the structural integrity of SOD in utZIF-SOD. Hence, utZIF-SOD could exhibit excellent stability in aged cells with high oxidative stress levels, rendering them to effectively resist oxidative stress and treat senile osteoporosis.

© 2024 Wiley-VCH GmbH

16163028, 0, Downloaded from https://onlinelibrary.wiley.com/doi/10.1002/adfm.202410931 by Cas-Beijing Institution Of, Wiley Online Library on [05/09/2024]. See the Terms and Conditions (https://onlinelibrary.wiley.com/terms-and-conditions) on Wiley Online Library for rules of use; OA articles are governed by the applicable Creative Commons License

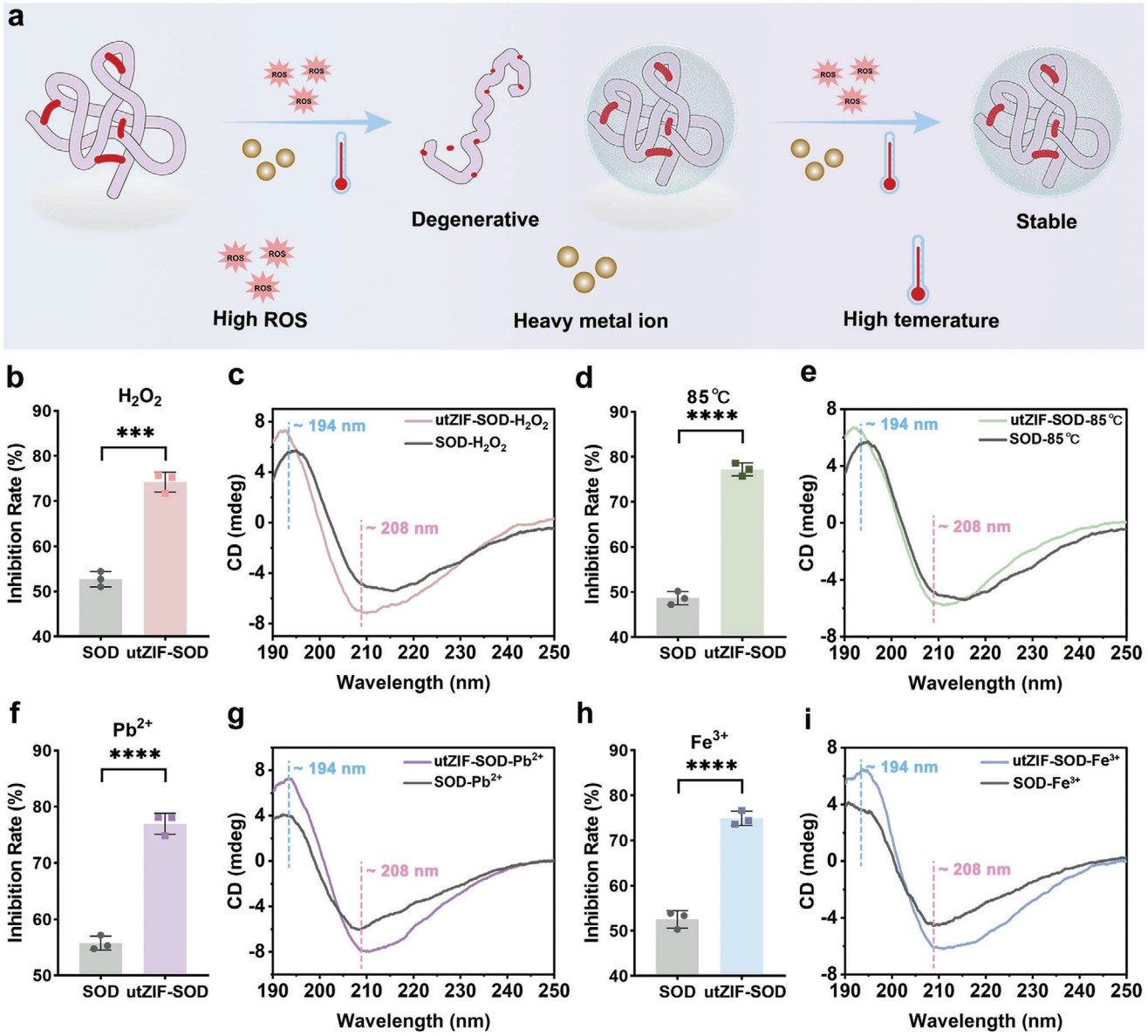

Figure 3. Catalytic activity and stability of utZIF-SOD. a) Schematic illustration of the utZIF-SOD stability. $O_2^{\bullet-}$-inhibition rates of native SOD and utZIF-SOD after b) high ROS concentration, d) 85 °C, f) Pb^{2+}, h) Fe^{3+} treatment. Data are expressed as mean ± standard deviation (SD) (n = 3). CD spectra demonstrating the secondary structures of native SOD after (c) high ROS concentration, (e) 85 °C, (g) Pb^{2+}, i) Fe^{3+} treatment. Student's t-test, $^*P < 0.05$, $^{**}P < 0.01$, $^{***}P < 0.001$, $^{****}P < 0.0001$, ns $P > 0.05$.

2.3. Biocompatibility and Internalization Pathway of utZIF-SOD

In order to better explore the biological characteristics of utZIF-SOD, we also synthesized SOD loaded on submicron scale ZIF-8 carrier (SOD@smZIF) with the size of about ≈100 nm (Figure S7, Supporting Information) and conducted comparative experiments. To quantitatively explore the therapeutic efficacy of native SOD, utZIF-SOD, and SOD@smZIF, we initially conducted the typical cell-counting kit 8 (CCK-8) protocol to evaluate in vitro cytotoxicity (**Figure** 4a–c). No significant decrease in cell viability was detected in the native SOD and utZIF-SOD group, even at a dose as high as 200 μg mL^{-1}. In contrast, the SOD@smZIF group showed a high cell death rate and significant cytotoxicity at concentrations as low as 50 μg mL^{-1}. Therefore, a concentration of containing 20 μg mL^{-1} SOD was selected for the subsequent experiments. Additionally, BMSCs co-incubated with native SOD, utZIF-SOD, and SOD@smZIF were co-stained with Calcein-AM (green: live cells) and PI (propidium iodide, red: dead cells), and then detected using confocal laser scanning microscopy (CLSM) (Figure S8, Supporting Information). Consistent with the results of CCK-8, obvious cell death occurred in the SOD@smZIF group, but almost no cell death occurred in the native SOD and utZIF-SOD group. The high cytotoxicity of the SOD@smZIF group might be related to the inflammation caused by its large size and high mechanical damage (Figure 4d)[47,48] In subsequent experiments, we used

© 2024 Wiley-VCH GmbH

16163028, 0, Downloaded from https://onlinelibrary.wiley.com/doi/10.1002/adfm.202410931 by Cas-Beijing Institution Of, Wiley Online Library on [05/09/2024]. See the Terms and Conditions (https://onlinelibrary.wiley.com/terms-and-conditions) on Wiley Online Library for rules of use; OA articles are governed by the applicable Creative Commons License

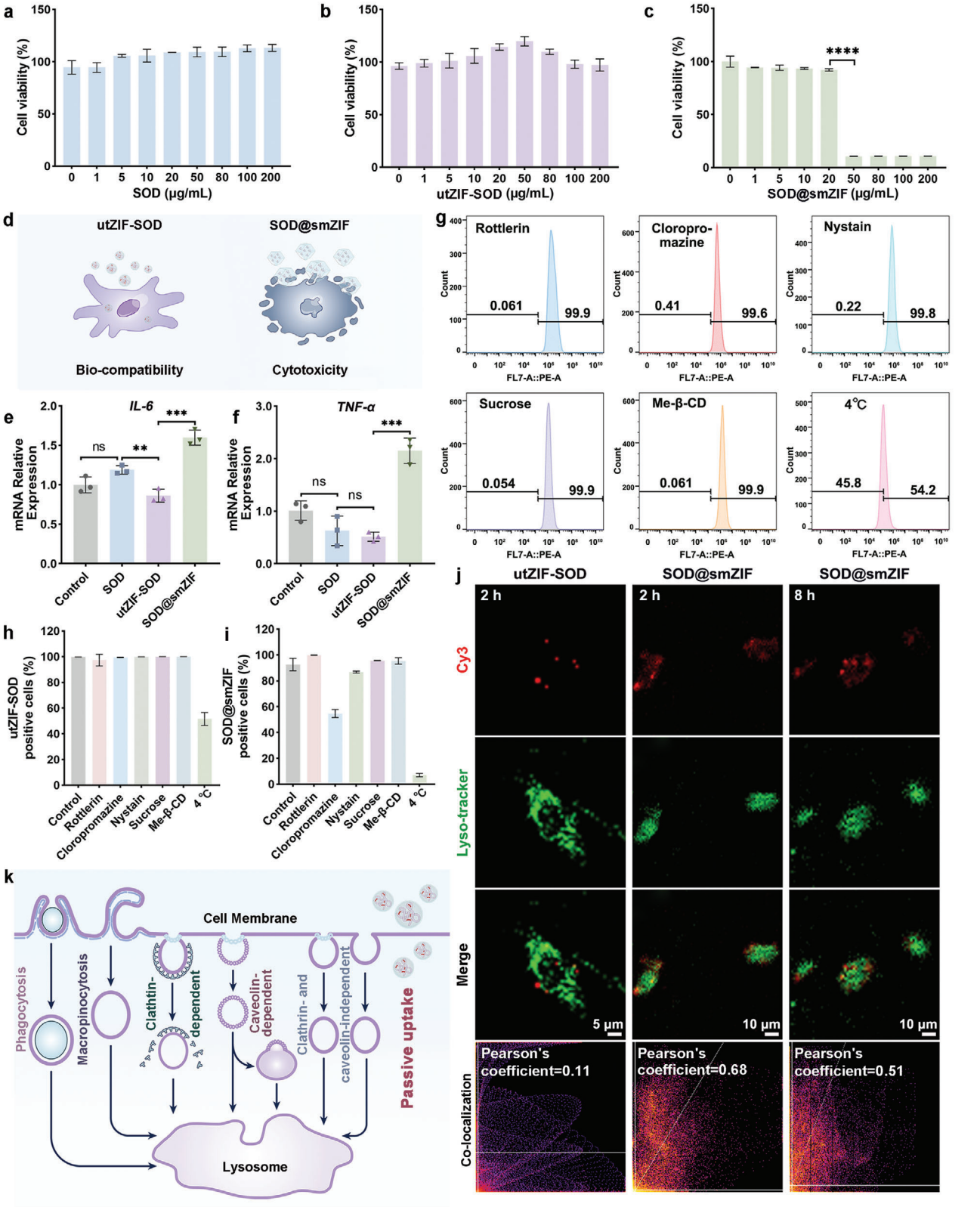

Figure 4. Biocompatibility and endocytosis pathway of utZIF-SOD. Cytotoxicity after treatment with a) native SOD, b) utZIF-SOD and c) SOD@smZIF at varied concentrations. d) Schematic diagram of cytotoxicity. Relative expression of mRNA levels of e) *IL-6* and f) *TNF-α* in aged BMSCs after different treatments. The quantification was made by qRT-PCR. g) The flow cytometry analysis of intracellular utZIF-SOD treated with various endocytosis inhibitors. Intracellular internalization statistics of h) utZIF-SOD and i) SOD@smZIF treated with various endocytosis inhibitors (Control: treated only

© 2024 Wiley-VCH GmbH

16163028, 0, Downloaded from https://onlinelibrary.wiley.com/doi/10.1002/adfm.202410931 by Cas-Beijing Institution Of, Wiley Online Library on [05/09/2024]. See the Terms and Conditions (https://onlinelibrary.wiley.com/terms-and-conditions) on Wiley Online Library for rules of use; OA articles are governed by the applicable Creative Commons License

16163028, 0, Downloaded from https://onlinelibrary.wiley.com/doi/10.1002/adfm.202410931 by Cas-Beijing Institution Of, Wiley Online Library on [05/09/2024]. See the Terms and Conditions (https://onlinelibrary.wiley.com/terms-and-conditions) on Wiley Online Library for rules of use; OA articles are governed by the applicable Creative Commons License

quantitative real-time polymerase chain reaction (qRT-PCR) to explore the changing trend of pro-inflammatory factors after BMSCs were treated with different groups. The expression levels of interleukin-6 (*IL-6*) (Figure 4e) and tumor necrosis factor-α (*TNF-α*) (Figure 4f) in the native SOD and utZIF-SOD group were similar to or lower than those in the control group, which indicated that the native SOD and utZIF-SOD group did not induce the inflammatory reaction in cells. On the contrary, due to SOD effectively scavenging ROS from cells, they showed a certain anti-inflammatory role. However, the levels of inflammatory factors in the SOD@smZIF group increased sharply, showing an obvious pro-inflammatory phenomenon. The above experimental results revealed that utZIF-SOD was a novel enzyme nanoformulation with high biocompatibility, which was more conducive to the study of protein delivery and enzyme catalysis.

Next, we studied the intracellular internalization pathway of utZIF-SOD, we initially labeled SOD with cyanine 3 (Cy3) to observe the intracellular delivery of utZIF-SOD (Cy3-utZIF-SOD). Various endocytosis inhibitors, including rottlerin (micropinocytosis inhibitor), chlorpromazine and sucrose (clathrin-mediated endocytosis inhibitor), nystatin (caveolae-mediated endocytosis inhibitor), and methyl-β-cyclodextrin (Me-β-CD, clathrin-independent endocytosis inhibitor) were employed to study the intracellular internalization pathway (Figure 4g, h; Figure S9a, Supporting Information). Comparing the internalization efficiency of Cy3-utZIF-SOD pretreated with and without endocytosis inhibitors, it was found that the intracellular delivery of Cy3-utZIF-SOD was not significantly inhibited. Additionally, the internalization of Cy3-utZIF-SOD when treatment was slightly limited at low temperature (4 °C), demonstrating no obvious energy dependence. This result indicated that the uptake route of Cy3-utZIF-SOD might not depend on surface-mediated proteins. Conversely, the intracellular delivery of Cy3-SOD@smZIF was significantly inhibited after chlorpromazine treatment, and the inhibition effect was more pronounced at 4 °C (Figure 4i, Figure S9b–h, Supporting Information), showing that the cell uptake of Cy3-SOD@smZIF was an energy-dependent, receptor-mediated endocytosis. After uptake through the endocytosis route, Cy3-SOD@smZIF eventually entered lysosomes, which would reduce the utilization efficiency of nanodrugs. Then, CLSM analysis showed that the accumulation of SOD in the cytosol was observed after treating BMSCs with Cy3-utZIF-SOD (containing 20 μg mL^{-1} SOD) for 2 h (Figure 4j). Additionally, the co-localization coefficient (Pearson's correlation coefficient) of Cy3-utZIF-SOD and lysosome in CLSM imaging was 0.11, indicating that Cy3-utZIF-SOD were not present in lysosomes. From the above results, it could be concluded that utZIF-SOD was internalized into cells mainly through passive uptake and would not enter lysosomes to avoid degradation (Figure 4k). On the contrary, after BMSCs were treated with Cy3-SOD@smZIF containing 20 μg mL^{-1} SOD for 8 h, the Pearson's correlation coefficient of Cy3-SOD@smZIF and lysosome was 0.51, which was lower than that after 2 h treatment (0.68) (Figure 4j), indicating that a certain amount of Cy3-SOD@smZIF could escape from lysosomes. Although Cy3-SOD@smZIF possessed the characteristics of lysosome escape, a significant number of Cy3-SOD@smZIF still remained in lysozyme, where the ZIF-8 shell and SOD structure were decomposed. In order to investigate the influence of lysosomal degradation on structure and function, we simulated the microenvironment of cytoplasmic matrix and lysosome with pH = 7.4 and pH = 5.3 buffers, respectively. Compared with the neutral buffer, the scavenging ROS ability of utZIF-SOD and SOD@smZIF treated with the acidic buffer decreased (Figure S10, Supporting Information), which was attributed to the decomposition of ZIF and deprotection of SOD in acidic environment, thereby resulting in the decrease or even inactivation of SOD.

2.4. In Vitro Biocatalysis and Cell Function of utZIF-SOD

After exploring the efficient cellular uptake of utZIF-SOD, we subsequently studied whether enzyme-encapsulated utZIF-SOD retained its intracellular biocatalytic activity in aged cells with high oxidative stress levels. To this end, we chose BMSCs that had grown to different generations, specifically the fifth generation (P5) and the tenth generation (P10). To observe the ROS content and the scavenging effect of utZIF-SOD during the aging process from youth to old age, BMSCs at P5 and P10 were first treated with native SOD, utZIF-SOD, and SOD@smZIF, and then stained with DCFH-DA (**Figure 5**a; Figure S11, Supporting Information). In the BMSCs at P5, which were relatively young, a small amount of ROS could be observed in the control group. After treatment with native SOD and utZIF-SOD, most of the ROS in the cells were removed, with no significant difference between the two groups. In the BMSCs at P10, which were in an aged state, higher ROS content was observed in the control group. Compared with native SOD, the utilization efficiency of utZIF-SOD effectively scavenged excess ROS was ≈1.5 times that of native SOD. This result might be attributed to the good protective effect of ZIF-8 shell on SOD in aged cells with high oxidative stress levels, which could effectively prevent SOD inactivation caused by high ROS.[49,50] This result was consistent with previous stability findings. Due to the high concentration of ROS inducing DNA damage, phosphorylation of Ser-139 of histone H2AX molecules (γ-H2AX), a common indicator of DNA damage, was examined in the subsequent experiments.[51] Compared to the control and SOD group, utZIF-SOD showed better DNA repair after treatment (Figure 5b,c). These results further indicated that the ultrathin ZIF-8 shell of utZIF-SOD could protect SOD from the damage caused by high ROS in aged cells, thus effectively scavenge ROS from aged cells and restore them to a relatively young state.

Since aging in BMSCs was associated with deteriorations in proliferation capacity, colony-formation ability, migration activity, and cell dryness,[52,53] we subsequently investigated whether utZIF-SOD had any influence on these biological characteristics of aged BMSCs. Senescence-associated β-galactosidase (SA-β-gal) staining revealed a decreased percentage of positive cells

with corresponding nanomaterials). BMSCs were pretreated with endocytosis inhibitors as indicated for 1 h before cellular delivery of utZIF-SOD or SOD@smZIF (containing 20 μg mL^{-1} SOD). CLSM images of BMSCs incubated with j) utZIF-SOD and SOD@smZIF containing 20 μg mL^{-1} SOD. Scale bars: 10 μm. k) Schematic diagram of utZIF-SOD internalization pathway. Data were expressed as mean ± standard deviation (SD) (n = 3). Analyzed by one-way ANOVA, *P < 0.05, **P < 0.01, ***P < 0.001, ****P < 0.0001, ns P > 0.05.

 © 2024 Wiley-VCH GmbH

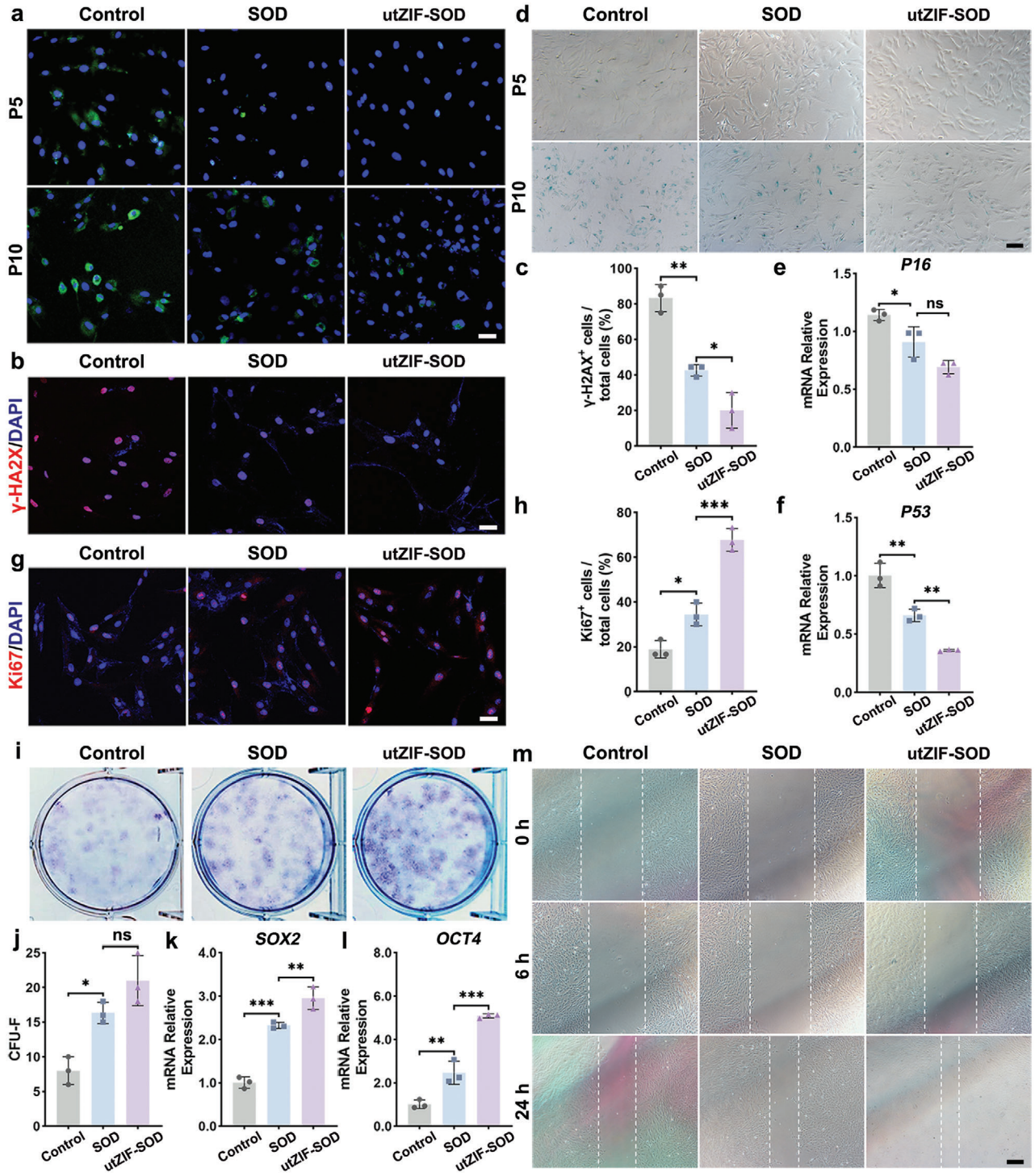

Figure 5. In vitro biocatalysis and cell function of utZIF-SOD. a) Confocal images of intracellular ROS levels of BMSCs stained with DCFH-DA oxidative stress indicator (green) and Hoechst 33342 (blue, nucleus) after different treatments. Scale bars: 200 μm. Immunofluorescence staining of b) γ-H2AX in aged BMSCs after different treatments. Scale bars: 200 μm. d) Representative images of senescence-associated β-galactosidase (SA-β-gal) staining of aged BMSCs. Scale bars: 200 μm. Relative expression of mRNA levels of e) *P16* and f) *P53* in aged BMSCs after different treatments. The quantification was made by qRT-PCR. Immunofluorescence staining of g) Ki67 in aged BMSCs after different treatments. Scale bars: 200 μm. i) Crystal violet staining of colony-forming units after different treatments of BMSCs. Semi-quantification of c) γ-H2AX derived from Data (b), h) Ki67 derived from Data (g) and j) colony-forming units derived from Data (i). Relative expression of mRNA levels of k) *OCT4* and l) *SOX2* in aged BMSCs after different treatments. The quantification was made by qRT-PCR. m) Scratch assay of aged BMSCs after different treatments. Magenta dotted lines indicated start (0 h), half (6 h), and end (24 h) positions of BMSCs after scraping. Scale bars: 200 μm. Data were expressed as mean ± standard deviation (SD) (n = 3). Analyzed by one-way ANOVA, $*P < 0.05$, $**P < 0.01$, $***P < 0.001$, $****P < 0.0001$, ns $P > 0.05$.

© 2024 Wiley-VCH GmbH

16163028, 0, Downloaded from https://onlinelibrary.wiley.com/doi/10.1002/adfm.202410931 by Cas-Beijing Institution Of, Wiley Online Library on [05/09/2024]. See the Terms and Conditions (https://onlinelibrary.wiley.com/terms-and-conditions) on Wiley Online Library for rules of use; OA articles are governed by the applicable Creative Commons License

in the utZIF-SOD group in aged BMSCs (Figure 5d; Figure S12, Supporting Information). Consistently, the expression of aging markers, such as *P16* and *P53*, was significantly down-regulated in response to utZIF-SOD treatment (Figure 5e,f). Furthermore, utZIF-SOD-treated aged BMSCs exhibited markedly elevated proliferation capacity, as indicated by the greater number of $Ki67^+$ cells (Figure 5g and h). Additionally, the colony formation assay showed that utZIF-SOD-treated aged BMSCs had a higher self-renewal capacity than other groups, evidenced by increases in the number and diameter of the colony-forming unit fibroblasts (CFU-Fs) (Figure 5i,j). Next, we investigated the migration of aged BMSCs through a scratch assay in the presence or absence of native SOD and utZIF-SOD. At 0, 6 and 24 h after scratching, the utZIF-SOD-treated group showed faster wound healing (Figure 5m; Figure S13, Supporting Information). The accumulation of ROS in the aging process affects the stemness of stem cell.[54] To observe whether utZIF-SOD could effectively improve the cell stemness of aged BMSCs, we used qRT-PCR to detect the expression level of cell stemness. After treatment with utZIF-SOD, the aged BMSCs showed more significant increases in the expression levels of *SOX2* (Figure 5k) and *OCT4* (Figure 5l).

2.5. Osteogenic Differentiation of utZIF-SOD Treated Aged BMSCs

To evaluate the effect of utZIF-SOD on osteogenic differentiation of aged BMSCs in vitro, we selected BMSCs cultured up to the tenth generation and subjected them to osteogenic induction medium. Compared to other groups, utZIF-SOD supplementation significantly increased alkaline phosphatase (ALP) activity after 7 d of osteogenic induction (**Figure 6**a,b) and enhanced the formation of mineralized nodules after 14 d (Figure 6c,d). Alizarin red staining also demonstrated that BMSCs derived from the utZIF-SOD treatment group formed more calcified nodules. Next, we assessed the expression of osteogenic-related genes, including BMP2 and RUNX2, in aged BMSCs induced in vitro using qRT-PCR (Figure 6e,f) and Western blotting (Figure 6g). Consistently, utZIF-SOD treatment upregulated the expression of osteogenic-related genes (BMP2 and RUNX2). Western blotting analysis showed that the autophagy-related marker LC3 was upregulated after utZIF-SOD treatment, indicating that utZIF-SOD regulated osteogenic differentiation by activating autophagy (Figure S14, Supporting Information). Aged cells not only lose normal cellular function but also disrupt the function of neighboring cells by secreting high levels of inflammatory cytokines.[55] In addition, ROS can promote the production of pro-inflammatory cytokines (such as *IL-1*, *IL-6*, and *TNF-α*), and further up-regulate the expression of ROS.[56] Therefore, effectively inhibiting inflammation can enhance the therapeutic effect of senile osteoporosis. Subsequently, we investigated whether utZIF-SOD could exert an anti-inflammatory effect in aged BMSCs. Inflammation in BMSCs was induced with lipopolysaccharide (LPS) and then treated with native SOD and utZIF-SOD, respectively. The levels of inflammatory factors *IL-1*, *IL-6*, and *TNF-α* decreased significantly after utZIF-SOD treatment, and even returned to the levels observed before LPS induction (Figure 6h–j). This effect was attributed to the effective scavenging of ROS by utZIF-SOD.

2.6. Senile Osteoporosis Treatment with utZIF-SOD

To study the therapeutic effect of utZIF-SOD on senile osteoporosis, we selected naturally senile mice, 18-month-old mice with evident osteoporosis, as animal models (**Figure 7**a). To determine the administration cycle, we initially injected Cy3-labeled SOD and utZIF-SOD into the senile mice via tail vein injection and observed the circulating half-life of native SOD and utZIF-SOD in the old mice. It was found that the fluorescence signal in mice was significantly weakened after 7 d of administration (Figure S15, Supporting Information). Therefore, we considered one week of treatment as a course of administration for treating osteoporosis in senile mice. Following 10 weeks of administration, we assessed the therapeutic effect of utZIF-SOD on senile osteoporosis (Figure 7b). MicroCT analysis revealed that, compared to the native SOD group, the bone mineral density (BMD) and vertebral bone volume (BV/TV) of osteoporosis mice in the utZIF-SOD treatment group markedly increased. Significantly, the BMD increment of utZIF-SOD was ≈2 times that of native SOD. Consistently, the trabecular thickness (Tb.Th) and trabecular number (Tb.N) increased, accompanied by a decrease in trabecular separation (Tb.Sp) (Figure 7c). Histomorphometric analysis further confirmed the increased bone mass, particularly in the utZIF-SOD group (Figure 7d). The crystal violet staining experiment showed that utZIF-SOD was more beneficial to maintain the formation of CFU-F (Figure 7e,f). Furthermore, utZIF-SOD effectively improved the cell stemness of BMSCs in osteoporotic mice (Figure 7g,h). As BMSCs played a crucial role during bone formation, we isolated BMSCs from treated mice to explore their osteogenic potential. After 7 d of osteogenic induction, utZIF-SOD significantly augmented ALP and ARS activity (Figure 7i–l). In addition, utZIF-SOD-treated BMSCs retained high expression levels of *Bmp2* and *Runx2*, whereas other treatment groups gradually lost the expression of these genes, as confirmed by Western blotting analysis and qRT-PCR (Figure 7m–o). The above results indicated that utZIF-SOD treatment restored the osteogenic differentiation ability of the BMSC populations in senile mice. H&E staining of major organs, including heart, liver, kidney and spleen, suggested no obvious necrosis, congestion, or hemorrhage, demonstrating the good biocompatibility of utZIF-SOD (Figure S16, Supporting Information).

3. Conclusion

Protein therapeutics play an essential role in the treatment of human diseases. Although many carriers have achieved the delivery of proteins, intracellular protein delivery remains a challenge. During internalization, these nanoparticles will be captured by the endo-lysosomal system, and restricted to endosomes/lysosomes with low pH and rich in acid hydrolase, triggering enzyme inactivation and limited therapeutic effects. Based on the scientific questions above, we constructed an ultrasmall enzyme nanoformulation reinforced with ultrathin ZIF-8 coating via an in situ coordination-mediated self-assembly strategy to avoid lysosomal degradation through passive uptake for senile osteoporosis therapy. Remarkably, utZIF-SOD achieved direct, efficient cellular uptake mediated by small size effect, thereby avoiding lysosomal degradation and exhibiting high delivery efficiency. Due to ultrathin ZIF-8 coating, utZIF-SOD exhibited

© 2024 Wiley-VCH GmbH

16163028, 0, Downloaded from https://onlinelibrary.wiley.com/doi/10.1002/adfm.202410931 by Cas-Beijing Institution Of, Wiley Online Library on [05/09/2024]. See the Terms and Conditions (https://onlinelibrary.wiley.com/terms-and-conditions) on Wiley Online Library for rules of use; OA articles are governed by the applicable Creative Commons License

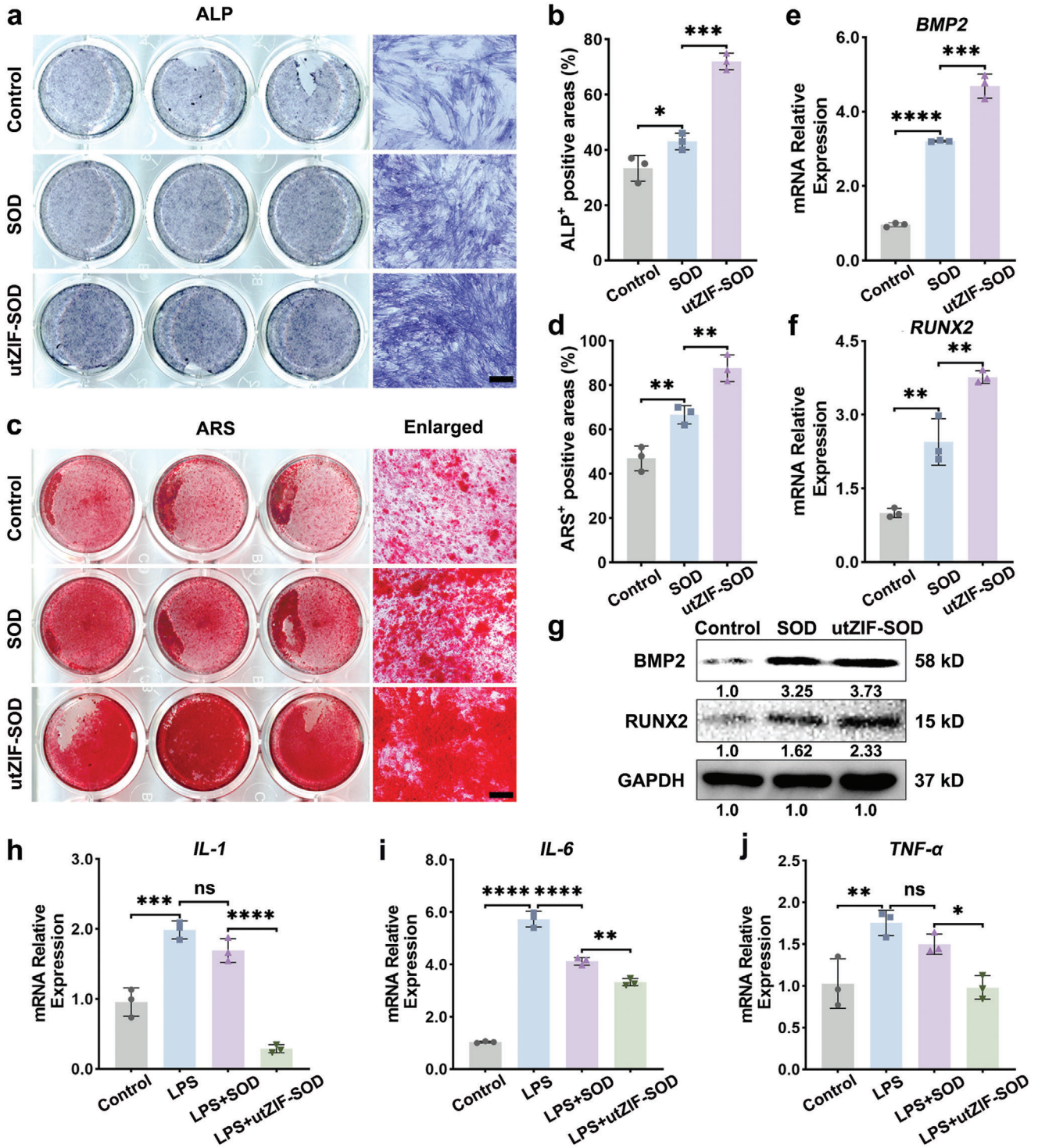

Figure 6. Anti-inflammatory effect and promotion of bone differentiation by utZIF-SOD on aged BMSCs. Representative images of a) ALP and c) ARS staining of aged BMSCs with different treatments. Scale bars: 200 μm. Semi-quantification of b) ALP derived from Data (a) and d) ARS derived from Data (c). Relative expression of mRNA levels of (e) *BMP2* and f) *RUNX2* in aged BMSCs after different treatments. The quantification was made by qRT-PCR. g) Western blot analyses of BMP2 and RUNX2 in aged BMSCs treated with different treatments. Relative expression of mRNA levels of h) *IL-1*, i) *IL-6* and j) *TNF-α* in LPS-activated aged BMSCs after different treatments. The quantification was made by qRT-PCR. Data were expressed as mean ± standard deviation (SD) (n = 3). Analyzed by one-way ANOVA, $^{*}P < 0.05$, $^{**}P < 0.01$, $^{***}P < 0.001$, $^{****}P < 0.0001$, ns $P > 0.05$.

© 2024 Wiley-VCH GmbH

16163028, 0, Downloaded from https://onlinelibrary.wiley.com/doi/10.1002/adfm.202410931 by Cas-Beijing Institution Of, Wiley Online Library on [05/09/2024]. See the Terms and Conditions (https://onlinelibrary.wiley.com/terms-and-conditions) on Wiley Online Library for rules of use; OA articles are governed by the applicable Creative Commons License

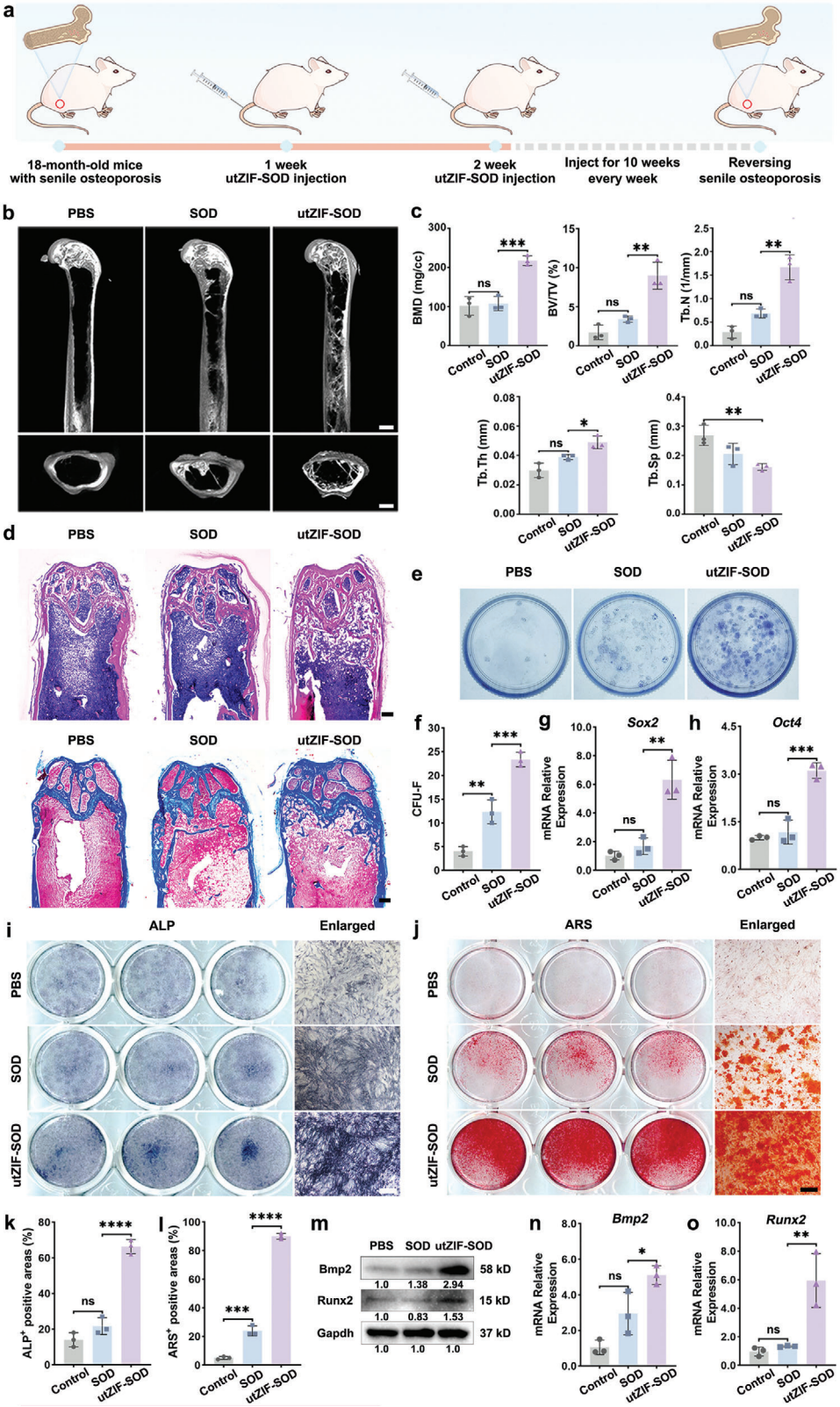

Figure 7. Senile osteoporosis treatment by utZIF-SOD. a) Treatment flow chart of senile mice with osteoporosis (3 groups, n = 3). b) Micro-CT reconstruction of femurs. Scale bar = 2 mm. c) Quantitative micro-CT analyses of distal femurs. d) Von Kossa and masson staining of demineralized femurs sections. Scale bar = 100 μm. e) Crystal violet staining of colony-forming units after different treatments of BMSCs. Semi-quantification of f) colony-forming units derived from Data (e). Relative expression of mRNA levels of g) *Oct4* and (h) *Sox2* in aged BMSCs of senile mice after different

© 2024 Wiley-VCH GmbH

16163028, 0, Downloaded from https://onlinelibrary.wiley.com/doi/10.1002/adfm.202410931 by Cas-Beijing Institution Of, Wiley Online Library on [05/09/2024]. See the Terms and Conditions (https://onlinelibrary.wiley.com/terms-and-conditions) on Wiley Online Library for rules of use; OA articles are governed by the applicable Creative Commons License

16163028, 0, Downloaded from https://onlinelibrary.wiley.com/doi/10.1002/adfm.202410931 by Cas-Beijing Institution Of, Wiley Online Library on [05/09/2024]. See the Terms and Conditions (https://onlinelibrary.wiley.com/terms-and-conditions) on Wiley Online Library for rules of use; OA articles are governed by the applicable Creative Commons License

excellent stability, even in the unamiable environment with high oxidative stress levels. It was demonstrated that ultrasmall enzyme nanoformulation reinforced with ultrathin ZIF-8 coating could promote osteogenic differentiation of aged BMSCs with high oxidative stress levels, and exhibited profound therapeutic efficacy against senile osteoporosis due to its potent stability and high uptake utilization rate in BMSCs. Overall, ultrasmall enzyme nanoformulation reinforced with ultrathin ZIF-8 coating via an in situ coordination-mediated self-assembly strategy, which bypasses the endo-lysosomal system during cellular entry, allows for potent protein delivery and robust therapy for senile osteoporosis.

4. Experimental Section

Chemicals, Materials, and Reagents: 1H-Imidazole-2-carboxylic acid (2-ICA), 1-(3-Dimethylaminopropyl)−3-ethylcarbodiimide hydrochloride (EDC), 2-Methylimidazole (2-MIM), Zinc nitrate hexahydrate ($Zn(NO_3)_2{\cdot}6H_2O$), Cyanine3 amine (Cy3-amine), Lead chloride ($PbCl_2$), Iron chloride ($FeCl_3$) and bovine erythrocytes Cu, Zn-SOD were obtained from Aladdin. SOD assay kit was purchased from Dojindo.

Preparation of utZIF-SOD: 2-ICA of 0.1 mg was dissolved in deionized water. Then, 0.14 mg of EDC was added to the solution. After the reaction at room temperature for 1 h, 5 mg of superoxide dismutase (SOD) was added and stirred for 2 h. Next, 1.5 mg of 2-MIM was added, and stirring continued for 10 min. Finally, 1.39 mg of $Zn(NO_3)_2{\cdot}6H_2O$ was added to react for 10 min. The utZIF-SOD was obtained by washing with ethanol three times and centrifuging.

Preparation of Cy3-utZIF-SOD: 2-ICA of 0.1 mg was dissolved in deionized water, and then 0.14 mg of EDC was added to the solution. After reacting at room temperature for 1 h, 5 mg of SOD was added and stirred for 2 h. Subsequently, another 0.14 mg of EDC was added to the solution. After 0.5 h, Cy3-amine was added, and the reaction was continued for 1 h. Then, 1.5 mg of 2-MIM was added and stirred for 10 min, followed by the addition of 1.39 mg of $Zn(NO_3)_2{\cdot}6H_2O$ for a reaction period of 10 min. Afterward, centrifugal washing was repeated to remove excess Cy3-amine. Finally, Cy3-utZIF-SOD was acquired.

Preparation of SOD@smZIF: SOD of 5 mg was added to the 2-MIM (0.29 g, 1 mL) water solution. The mixture was stirred at room temperature for 20 min. Subsequently, $Zn(NO_3)_2{\cdot}6H_2O$ (13.4 mg) was added and allowed to react for an additional 20 min. After centrifugal washing with ethanol, SOD@smZIF was obtained.

Preparation of Cy3-SOD@smZIF: SOD of 5 mg was dissolved in deionized water. Then, 0.14 mg of EDC was added to the solution. After a 0.5 h reaction at room temperature, 2-MIM (0.29 g, 1 mL) in water solution was added. The mixture was stirred at room temperature for 20 min. Subsequently, $Zn(NO_3)_2{\cdot}6H_2O$ (13.4 mg) was added and allowed to react for an additional 20 min. After centrifugal washing with ethanol, Cy3-SOD@smZIF was obtained.

Material Characterization: TEM investigations were obtained using FEI Tecnai G2 F20. Meanwhile, the elemental mapping analysis was determined using EDX. The height and Young's modulus of nanosheet were tested by AFM (Dimension Icon, Bruker, USA) under the Peakforce QNM mode using TAP150-G silicon cantilever. The acquired images, with 512×512 pixels, were analyzed using a NanoScope software version 3.00. DLS experiments were carried out with Zetasizer Nano instrument (Malvern Instruments Ltd., UK). FTIR spectra of native SOD, utZIF-SOD and ZIF-8 were recorded on a Bruker VERTEX80v FTIR spectrometer using KBr pellets. XRD data were collected using a Panalytical Xpert3 Powder X-ray diffractometer with Cu Kα ($\lambda = 0.15406$ nm). XPS measurements were performed with a Thermo Scientific K-Alpha spectrometer, and the shift of binding energy due to relative surface charge was corrected using the C 1s spectrum at 284.8 eV. CD measurements (190–250 nm) were conducted with a Jasco J-1500 CD spectrometer in a quartz cuvette with a 1 cm path length. For the measurements, the protein concentration was adjusted to 0.02 mg mL^{-1}. Each sample was scanned three times at a scanning speed of 50 nm/min with a bandwidth of 1 nm.

Enzymatic Activity and Stability Assay: The SOD activity of clusterzymes was tested according to the description in the SOD Activity Assay Kit. The environment with high levels of ROS was simulated by adding an excess of pyrogallol. After SOD or utZIF-SOD was treated at 85 °C, Pb^{2+} or Fe^{3+} for 30 min, the inhibition rate of $O_2^{\bullet-}$ of SOD and utZIF-SOD was determined, respectively.

Cell Culture: Human BMSCs (PCS-500-012) were purchased from Beijing Zhongyuan Company Limited (Beijing, China) and cultured with α-MEM medium (Invitrogen, Carlsbad, CA, United States) with 15% fetal bovine serum (Gibco, MA, United States) and 1% Penicillin/Streptomycin (Gibco, MA, United States). During the incubation, the temperature at 37 °C was kept, the humidity at 95%, and the CO_2 concentration at 5%. Primary cells were cultured to different generations for further experiments in vitro.

Cytotoxicity Assay (CCK8): The cytotoxicity of SOD, utZIF-SOD and SOD@smZIF against BMSCs was evaluated using the Cell Counting Kit-8 assay (CCK-8). Briefly, BMSCs were seeded in 96-well plates at a density of 5000 cells mL^{-1} for 24 h. Subsequently, fresh media with SOD, utZIF-SOD or SOD@smZIF (0 – 200 μg mL^{-1}) was replaced and incubated for 24 h. 10 μL of CCK-8 solution (LJ621, Dojindo, Japan) was then added into each well and incubated for 2 h before measuring the absorbance at 450 nm using a using a microplate reader (Bio-Rad).

Propidium Iodide (PI)/Calcein-AM Staining: The PI/Calcein-AM double stain kit (CA1630, Solarbio) was used to detect cell apoptosis. After the SOD, utZIF-SOD and SOD@smZIF (containing 20 μg mL^{-1} SOD) treatment for 24 h, BMSCs were incubated with 10 μM Calcein-AM and 10 μM PI at 37 °C for 20 min. CLSM images were captured using a laser-scanning microscope (LSM510, Zeiss, Germany) and processed with LSM 5 Release 4.2 software. Live cells were observed using a 490 nm excitation filter, while dead cells were observed using a 545 nm excitation filter.

Cellular Uptake and Intracellular Distribution Study of Cy3-utZIF-SOD and Cy3-SOD@smZIF: For the cellular uptake study of utZIF-SOD and SOD@smZIF, BMSCs were seeded at a density of 2.5×10^4 cells per well in 6-well plates 24 h prior to the experiment. Subsequently, cells were incubated with different concentrations of Cy3-utZIF-SOD/Cy3-SOD@smZIF for 8 h. At the end of incubation period, the cells were washed twice with PBS and harvested for flow cytometry analysis. To further investigate the endocytosis pathway of Cy3-utZIF-SOD, BMSCs were pre-treated with various endocytosis inhibitors, including 10 μM rottlerin, 20 μM Cloropromazine, 20 μM nystatin, 0.6 M sucrose, and 3 mM Me-β-CD, for 1 h. Subsequently, Cy3-utZIF-SOD/Cy3-SOD@smZIF (containing 20 μg mL^{-1} SOD) was added, and the cells were further incubated for 8 h before flow cytometry analysis as described above. For the cellular distribution study of Cy3-utZIF-SOD, BMSCs were seeded at a density of 1.5×10^4 cells in confocal dish 24 h prior to the experiment. The cells were incubated with Cy3-utZIF-SOD/Cy3-SOD@smZIF (containing 20 μg mL^{-1} SOD) for 2 h or 8 h at 37 °C. At the end of incubation, the cells were washed with PBS twice and incubated with 100 nM Lyso-Tracker Green (C1047S, Beyotime) for 1hours at 37 °C. Subsequently, the cells were washed twice with PBS before CLSM imaging.

Measurement of ROS: Intracellular ROS levels were measured using the DCFH-DA oxidative stress indicator (Beyotime, S0033) following the manufacturer's instructions. Briefly, BMSCs treated under different conditions were incubated with serum-free medium containing 10 mM

treatments. The quantification was made by qRT-PCR. Representative images of i) ALP and j) ARS staining of the extracted BMSCs of senile mice with different treatments. Scale bar = 200 μm. Semi-quantification of k) ALP derived from Data (i) and l) ARS derived from Data (j). m) Western blot analyses of Bmp2 and Runx2 in the extracted BMSCs treated with different treatments. Relative expression of mRNA levels of n) *Bmp2* and o) *Runx2* in aged BMSCs of senile mice after different treatments. The quantification was made by qRT-PCR. Data were expressed as mean ± standard deviation (SD) (n = 3). Analyzed by one-way ANOVA, $^*P < 0.05$, $^{**}P < 0.01$, $^{***}P < 0.001$, $^{****}P < 0.0001$, ns $P > 0.05$.

 © 2024 Wiley-VCH GmbH

DCFH-DA at 37 °C for 30 min in the dark. Subsequently, the cells were washed twice with serum-free medium and resuspended in α-MEM medium supplemented with Hoechst 33342 (C1027, Beyotime, China). Finally, the cells were harvested, and fluorescence signals were assessed at 488/525 nm using fluorescent microscopy (Leica, Germany) and analyzed using Image-Pro Plus 6.0 software (Media Cybernetics, MD, USA).

Senescence-Associated β-galactosidase (SA-β-gal) Assay: The aging-related β-galactosidase (SA-β-gal) activity was assessed using the cell aging assay kit (KAA002, Millipore) in treated aged and young fibroblasts after 2 d of culture. SA-βGAL activity was also measured in BMSCs treated with high (50 ng mL^{-1}) or low (0.5 ng mL^{-1}) cytokine concentration or SCM for 5 or 10 d. In short, cells were inoculated in triplicate in a 24-well plate, washed twice with PBS 1×, and then fixed in formalin at room temperature for 5 min. Next, the cells were washed twice with PBS 1× and incubated with β-gal substrate in acidic buffer (pH = 6.0) at 37 °C overnight. The cells were then examined using an inverted microscope (NIKON TS100) and photographed. The appearance of perinuclear blue indicates that cells were aged.

Migration Assay: To evaluate the cell migration property after SOD, utZIF-SOD and SOD@smZIF treatment, BMSCs were seeded onto 6-well plates and allowed to grow in a monolayer for 24 h. Subsequently, a sterile 100–200 µL pipette tip was held vertically to scratch a cross in each well. The detached cells were then removed by washing with PBS and SOD, utZIF-SOD and SOD@smZIF were added in α-MEM to treat BMSCs. After 24 h, cell migration was observed using an optical microscope (Olympus, Japan).

Immunocytofluorescense Staining: Cells were fixed in 4% paraformaldehyde and permeabilized with 0.1% Triton X-100 at room temperature for 10 min. Next, the cells were incubated with 5% Bovine Serum Albumin (BSA) at room temperature for 1 h, followed by incubation with primary antibodies, including anti-γ-HA2X (ab81299, abcam), anti-Ki67 (AF0198, Affinity) at 4 °C overnight. After thoroughly washed, the cells were then incubated with tetramethylrhodamine isothiocyanate-conjugated secondary antibodies (1: 200, Zhongshan Golden Bridge Biotechnology, Beijing, China) in the dark for 1 h. Nuclei were counterstained with DAPI (P0131, Beyotime, China). Images were captured by using a laser-scanning microscope (LSM510, Zeiss, Germany). The fluorescence intensity was analyzed by using ImageJ software.

Colony-Formation Assay: BMSCs were plated in 6-well plates and the medium was replaced every 2–3 d. The medium containing SOD, utZIF-SOD or SOD@smZIF was added until cell colonies were observed under a microscope. At the end of the experiment, cells were fixed with 4% PFA (Sigma) and stained using the 0.1% Crystal Violet Solution. Colonies consisting of more than 50 cells were defined as single colony clusters, and the number of clusters was counted.

In Vitro osteogenic Differentiation of BMSCs: The osteogenic differentiation medium for BMSCs was prepared as described below: 10 nmol L^{-1} dexamethasone, 100 µmol L^{-1} ascorbic acid 2-phosphate and 10 mmol L^{-1} β-glycerophosphate were added to the α-MEM medium. BMSCs were then cultured in the obtained osteogenic differentiation medium for 14 d. Alizarin red S staining (Sigma) was performed to observe the calcium nodules formed during osteogenic process, following the manufacturer's instructions. Additionally, after culturing in osteogenic medium for 7 d, the cells were fixed in 4% PFA and stained using the ALP staining kit (Beyotime, P0321S) at room temperature, following the manufacturer's instructions.

Quantitative Reverse Transcription Polymerase Chain Reaction (qRT-PCR): Total RNA was extracted using TRIzol reagent (Invitrogen, Carlsbad, CA, United States) according to the manufacturer's instructions. RNA was then reverse transcribed into complementary first-strand cDNA using cDNA synthesis kits (Takara Bio, Inc., Otsu, Japan). Real-time PCR was subsequently performed using the FastStart Universal SYBR Green master kit (Roche) on an Applied Biosystems 7500 Real-Time PCR System (Life Technologies Corporation, United States) to determine the relative mRNA expression level. The primers sequences were designed using Primer Premier 5.0 software and were listed as follows:

hBMP2-F	ACTACCAGAAACGAGTGGGAA
hBMP2-R	GCATCTGTTCTCGGAAAACCT
hRUNX2-F	CACTGGCGCTGCAACAAGA
hRUNX2-R	CATTCCGGAGCTCAGCAGAATAA
h*IL-1*-F	TTCGACACATGGGATAACGAGG-
h*IL-1*-R	TTTTTGCTGTGAGTCCCGGAG
h*IL-6*-F	GGAGACTTGCCTGGTGAAAA
h*IL-6*-R	GTCAGGGGTGGTTATTGCAT
h*TNF-α*-F	CGCCACCACGCTCTTCTG
h*TNF-α*-R	GGCTACAGGCTTGTCACTCG
hGAPDH-F	TGCCACTCAGAAGACTGTGG
hGAPDH-R	TTCAGCTCTGGGATGACCTT

Western Blotting: BMSCs were harvested and lysis with RIPA buffer (Thermo Fisher Scientific) mixed with 1 mM PMSF (Beyotime, ST506). The protein concentrations were measured using BCA Protein Assay Kit (Beyotime, P0012S), and the 30 µg total protein was separated by 10% SDS-polyacrylamide gel and then transferred onto a polyvinylidene difluoride (PVDF) membrane (Millipore). After being blocked in 5% non-fat milk for 1 h at room temperature, the membranes were incubated overnight at 4 °C with the following primary antibodies: anti-BMP2 (ab284387, Abcam), anti-RUNX2 (12 556, cell signaling technology), and anti-GAPDH (AF7021, Affinity). Subsequently, the membranes were incubated with horseradish peroxidase-conjugated rabbit IgG (1: 5000, Zhongshanjinqiao), and protein bands were detected by enhanced with a SuperSignal West Pico Chemiluminescent Substrate (Thermo Fisher Scientific).

Animals: C57BL/6J mice aged 18 months were purchased from the Beijing Weitong Lihua Experimental Animal Center. All the experimental procedures in this study were conducted in line with animal welfare ethical regulations and approved by the Animal Use and Care Committee of Peking University (LA2023323). Since this study could not to determine the animal sample size needed for the experiment by the methods needed for efficacy analysis. Therefore, an alternative "resource equation" approach was adopted, which sets an acceptable range of degrees of freedom (DFs) to determine the sample size.[57] To achieve a DF in the range from 10 to 20, the minimum number of each experimental group was 2.67, while the maximum number of each group was 4.33.[58] In addition, in in vitro experiments, the designed utZIF-SOD showed excellent biological effects. Therefore, in the in vivo study, n = 3 was used for each group, which follows the 3R principle of animal sample size calculation (Reduction, Refinement, and Replacement). All mice were maintained under specific pathogen-free rooms with a 12-h light/12-h dark cycle. The animals were allowed access to free food pellets and tap water ad libitum. Animals were randomly divided into different groups, including control group (saline), SOD group (50 µg m^{-1} L SOD of saline sodium, 200 µL), utZIF-SOD group (50 µg mL^{-1} utZIF-SOD of saline sodium, 200 µL). The therapeutics were injected via a tail vein once a week for a total of 10 weeks. At the endpoint, all animals were sacrificed by excessive anesthesia, and internal organs (heart, liver, kidney, spleen) and femora were collected for analysis.

Isolation and Culture of Mice BMSCs: BMSCs were isolated from aged mice belonging to the control group, SOD group, and utZIF-SOD group, respectively. The mice were euthanized, and their bones were dissected and washed in sterile PBS. BMSCs was flushed out using a 25-gauge needle into α-MEM supplemented with 10% FBS and 1% penicillin/streptomycin. Upon reaching 70–80% confluence, BMSCs were passaged and plated in 6-well or 12-well plates for experiments.

Biodistribution Study of Therapeutics: To better understand the biodistribution of SOD and utZIF-SOD, they were conjugated with Cy3 and injected into healthy mice via the tail vein. At each time point (1 h, 1 d, 3 d, 7 d after injection), three mice in each group were anesthetized and subjected to vitro imaging using an IVIS Spectrum In Vivo Imaging System (PerkinElmer).

© 2024 Wiley-VCH GmbH

16163028, 0, Downloaded from https://onlinelibrary.wiley.com/doi/10.1002/adfm.202410931 by Cas-Beijing Institution Of, Wiley Online Library on [05/09/2024]. See the Terms and Conditions (https://onlinelibrary.wiley.com/terms-and-conditions) on Wiley Online Library for rules of use; OA articles are governed by the applicable Creative Commons License

μCT Scanning and Analysis: The mice femora were fixed in 10% paraformaldehyde for 24 h and scanned by with a Skyscan 1174 micro-CT system (Bruker, Belgium) at a resolution of 5.9 μm. The acquired axial images were imported into NRecon and CTvox software for visualization and analysis. The region of interest (ROIs) were defined as the areas 0.5-1 mm distal to the proximal epiphysis to include the secondary trabecular spongiosa. Bone mineral density (BMD), bone volume fraction (BV/TV), trabecular number (Tb.N), trabecular separation (Tb.Sp), and trabecular thickness (Tb.Th) were calculated within the ROIs using CTAn software.

Histomorphometric Analyses: The fixed femora were demineralized in 15% ethylenediaminetetraacetic acid (EDTA) and embedded in paraffin. Consecutive 4-μm-thick sections were obtained from each group and stained with haematoxylin and eosin (H&E) as well as Masson's trichrome staining, following the manufacturer's instructions. Similarly, the fixed internal organs (heart, liver, kidney, spleen) were embedded in paraffin. Consecutive 4-μm-thick sections were obtained from each group and stained with H&E.

Statistical Analysis: Statistical analysis was conducted using GraphPad Prism 8 (GraphPad Software). All data were expressed as mean ± SD. Comparison of means between two groups was performed using the Student's t test. For multiple comparison, one-way analysis of variance (ANOVA) was used to assess difference in means among groups. Differences of $*P < 0.05$, $**P < 0.01$, $***P < 0.001$ and $****P < 0.0001$ were considered statistically significant.

Supporting Information

Supporting Information is available from the Wiley Online Library or from the author.

Acknowledgements

This work was supported by the National Key Research and Development Program of China (2022YFB3205602), National Natural Science Foundation of China (52372174, 82230030, T2125003), Beijing International Science and Technology Cooperation Project (No. Z221100002722003), Beijing Natural Science Foundation (L234017, JL23002, L212010), Key R & D Plan of Ningxia Hui Autonomous Region (No. 2020BCG01001), Innovative Research Team of High-level Local Universities in Shanghai SHSMU-ZLCX20212402, and Clinical Medicine Plus X – Young Scholars Project of Peking University.

Conflict of Interest

The authors declare no conflict of interest.

Author Contributions

S.L., L.C., and C.L. contributed equally to this work. S.L., L.C., C. L. contributed to data acquisition and interpretation, performed all statistical analyses, drafted and critically revised the manuscript; B.G., and Y.F. contributed to data acquisition and analysis, critically revised the manuscript; Z.L., Y.L., and D.L. contributed to conception, design, data acquisition and interpretation, drafted and critically revised the manuscript. All authors gave their final approval and agree to be accountable for all aspects of the work.

Data Availability Statement

The data that support the findings of this study are available from the corresponding author upon reasonable request.

Keywords

enzyme nanoformulation, lysosomal degradation, passive uptake, senile osteoporosis, ultrathin ZIF-8 coating

Received: June 22, 2024
Revised: August 16, 2024
Published online:

[1] I. R. Reid, E. O. Billington, *Lancet* **2022**, *399*, 1080.
[2] Y. He, L. Zhang, X. Chen, B. Liu, X. Shao, D. Fang, J. Lin, N. a. Liu, Y. Lou, J. Qin, Q. Jiang, B. Guo, *Adv. Healthcare Mater.* **2023**, *13*, 2302972.
[3] J. S. Kimball, J. P. Johnson, D. A. Carlson, *J. Bone Joint Surg.* **2021**, *103*, 1451.
[4] D. A. Callaway, J. X. Jiang, *J. Bone Miner. Metab.* **2015**, *33*, 359.
[5] K. e. Li, S. Hu, J. Huang, Y. u. Shi, W. Lin, X. Liu, W. Mao, C. Wu, C. Pan, Z. Xu, H. Wang, L. Gao, H. Chen, *Nano Today* **2023**, *50*, 101839.
[6] D. Salvemini, D. P. Riley, S. Cuzzocrea, *Nat. Rev. Drug Discovery* **2002**, *1*, 367.
[7] T. Gui, L. Luo, B. Chhay, L. Zhong, Y. Wei, L. Yao, W. Yu, J. Li, C. L. Nelson, A. Tsourkas, L. Qin, Z. Cheng, *Biomaterials* **2022**, *283*, 121437.
[8] J. Zhou, M. Li, Q. Chen, X. Li, L. Chen, Z. Dong, W. Zhu, Y. Yang, Z. Liu, Q. Chen, *Nat. Commun.* **2022**, *13*, 3432.
[9] J. Hwang, J. Jin, S. Jeon, S. H. Moon, M. Y. Park, D.-Y. Yum, J. H. Kim, J.-E. Kang, M. H. Park, E.-J. Kim, J.-G. Pan, O. Kwon, G. T. Oh, *Redox Biol.* **2020**, *37*, 101760.
[10] R. Yan, J. Ren, J. Wen, Z. Cao, D. i. Wu, M. Qin, D. Xu, R. Castillo, F. Li, F. Wang, Z. Gan, C. Liu, P. Wei, Y. Lu, *Adv. Mater.* **2022**, *34*, 2105670.
[11] X. Qin, C. Yu, J. Wei, L. Li, C. Zhang, Q. Wu, J. Liu, S. Q. Yao, W. Huang, *Adv. Mater.* **2019**, *31*, 1902791.
[12] S. Mitragotri, P. A. Burke, R. Langer, *Nat. Rev. Drug Discovery* **2014**, *13*, 655.
[13] M. Yan, J. Du, Z. Gu, M. Liang, Y. Hu, W. Zhang, S. Priceman, L. Wu, Z. Zhou, Z. Liu, T. Segura, Y. Tang, Y. Lu, *Nat. Nanotechnol.* **2010**, *5*, 4.
[14] B. Leader, Q. J. Baca, D. E. Golan, *Nat. Rev. Drug Discovery* **2008**, *7*, 21.
[15] M. Wang, J. A. Zuris, F. Meng, H. Rees, S. Sun, P. Deng, Y. Han, X. Gao, D. Pouli, Q. i. Wu, I. Georgakoudi, D. R. Liu, Q. Xu, *Proc. Natl Acad. Sci.* **2016**, *113*, 2868.
[16] D. S. D'Astolfo, R. J. Pagliero, A. Pras, W. R. Karthaus, H. Clevers, V. Prasad, R. J. Lebbink, H. Rehmann, N. Geijsen, *Cell* **2015**, *161*, 674.
[17] M. M. Pakulska, S. Miersch, M. S. Shoichet, *Science* **2016**, *351*, aac4750.
[18] T. T. Chen, *J. Am. Chem. Soc.* **2018**, *140*, 9912.
[19] A. Kirchon, L. Feng, H. F. Drake, E. A. Joseph, H.-C. Zhou, *Chem. Soc. Rev.* **2018**, *47*, 8611.
[20] G. Song, Y. Shi, S. Jiang, H. Pang, *Adv. Funct. Mater.* **2023**, *33*, 2303121.
[21] J. Y. Oh, E. Choi, B. Jana, E. M. Go, E. Jin, S. Jin, J. Lee, J.-H. Bae, G. Yang, S. K. Kwak, W. Choe, J.-H. Ryu, *Small* **2023**, *19*, 2300218.
[22] B. Li, H.-M. Wen, Y. Cui, W. Zhou, G. Qian, B. Chen, *Adv. Mater.* **2016**, *28*, 8819.
[23] L. Niu, T. Wu, M. Chen, L. Yang, J. Yang, Z. Wang, A. A. Kornyshev, H. Jiang, S. Bi, G. Feng, *Adv. Mater.* **2022**, *34*, 2200999.
[24] S. Zhou, F. Jia, Y. Wei, J. Du, J. Liu, W. Dong, J. Sui, W. Xue, Y. Yang, L. Chen, X. Meng, S. Yu, *Adv. Funct. Mater.* **2024**, *34*, 2314012.
[25] S. Wang, W. Morris, Y. Liu, C. M. McGuirk, Y. Zhou, J. T. Hupp, O. K. Farha, C. A. Mirkin, *Angew. Chem., Int. Ed.* **2015**, *54*, 14738.

© 2024 Wiley-VCH GmbH

16163028, 0, Downloaded from https://onlinelibrary.wiley.com/doi/10.1002/adfm.202410931 by Cas-Beijing Institution Of, Wiley Online Library on [05/09/2024]. See the Terms and Conditions (https://onlinelibrary.wiley.com/terms-and-conditions) on Wiley Online Library for rules of use; OA articles are governed by the applicable Creative Commons License

[26] M. Yang, W. Xu, Z. Chen, M. Chen, X. Zhang, H. He, Y. Wu, X. Chen, T. Zhang, M. Yan, J. Bai, C. McAlinden, K. M. Meek, J. Yu, S. Ding, R. Gao, J. Huang, X. Zhou, *Adv. Mater.* **2022**, *34*, 2109865.
[27] J. Della Rocca, D. Liu, W. Lin, *Acc. Chem. Res.* **2011**, *44*, 957.
[28] Z. Zhou, M. Vázquez-González, I. Willner, *Chem. Soc. Rev.* **2021**, *50*, 4541.
[29] J. Matusiak, A. Przekora, W. Franus, *Mater. Today* **2023**, *67*, 495.
[30] E. Linnane, S. Haddad, F. Melle, Z. Mei, D. Fairen-Jimenez, *Chem. Soc. Rev.* **2022**, *51*, 6065.
[31] M. S. de Almeida, E. Susnik, B. Drasler, P. Taladriz-Blanco, A. Petri-Fink, B. Rothen-Rutishauser, *Chem. Soc. Rev.* **2021**, *50*, 5397.
[32] S. K. Alsaiari, S. Patil, M. Alyami, K. O. Alamoudi, F. A. Aleisa, J. S. Merzaban, M. o. Li, N. M. Khashab, *J. Am. Chem. Soc.* **2018**, *140*, 143.
[33] X. Yang, Q. Tang, Y. Jiang, M. Zhang, M. Wang, L. Mao, *J. Am. Chem. Soc.* **2019**, *141*, 3782.
[34] N. Liédana, A. Galve, C. Rubio, C. Tellez, J. Coronas, *ACS Appl. Mater. Interfaces* **2012**, *4*, 5016.
[35] Z. Liang, Z. Yang, H. Yuan, C. Wang, J. Qi, K. Liu, R. Cao, H. Zheng, *Dalton Trans.* **2018**, *47*, 10223.
[36] X. L. Wei, Z. Q. Ge, *Carbon* **2013**, *60*, 401.
[37] F. Secundo, *Chem. Soc. Rev.* **2013**, *42*, 6250.
[38] X. Wang, N. Fu, J.-C. Liu, K. Yu, Z. Li, Z. Xu, X. Liang, P. Zhu, C. Ye, A. Zhou, A. Li, L. Zheng, L.-M. Liu, C. Chen, D. Wang, Q. Peng, Y. Li, *J. Am. Chem. Soc.* **2022**, *144*, 23223.
[39] P. Deria, J. E. Mondloch, O. Karagiaridi, W. Bury, J. T. Hupp, O. K. Farha, *Chem. Soc. Rev.* **2014**, *43*, 5896.
[40] M. Mariconti, L. Dechamboux, M. Heckmann, J. Gros, M. Morel, V. Escriou, D. Baigl, C. Hoffmann, S. Rudiuk, *J. Am. Chem. Soc.* **2024**, *146*, 5118.
[41] L. Wang, B. Zhu, Y. Deng, T. Li, Q. Tian, Z. Yuan, L. Ma, C. Cheng, Q. Guo, L. Qiu, *Adv. Funct. Mater.* **2021**, *31*, 2101804.
[42] J. Tsay, Z. Yang, F. P. Ross, S. Cunningham-Rundles, H. Lin, R. Coleman, P. Mayer-Kuckuk, S. B. Doty, R. W. Grady, P. J. Giardina, A. L. Boskey, M. G. Vogiatzi, *Blood* **2010**, *116*, 2582.
[43] P. Mitra, S. Sharma, P. Purohit, P. Sharma, *Crit. Rev. Clin. Lab. Sci.* **2017**, *54*, 506.
[44] Y. Johmura, T. Yamanaka, S. Omori, T.-W. Wang, Y. Sugiura, M. Matsumoto, N. Suzuki, S. Kumamoto, K. Yamaguchi, S. Hatakeyama, T. Takami, R. Yamaguchi, E. Shimizu, K. Ikeda, N. Okahashi, R. Mikawa, M. Suematsu, M. Arita, M. Sugimoto, K. I. Nakayama, Y. Furukawa, S. Imoto, M. Nakanishi, *Science* **2021**, *371*, 265.
[45] J. J. Rennick, C. J. Nowell, C. W. Pouton, A. P. Johnston, *Nat. Commun.* **2022**, *13*, 6023.
[46] R. Murty, M. K. Bera, I. M. Walton, C. Whetzel, M. R. Prausnitz, K. S. Walton, *J. Am. Chem. Soc.* **2023**, *145*, 7323.
[47] N. Egge, S. L. Arneaud, R. S. Fonseca, K. R. Zuurbier, J. McClendon, P. M. Douglas, *Nat. Commun.* **2021**, *12*, 1484.
[48] J. M. J. Romac, R. A. Shahid, S. M. Swain, S. R. Vigna, R. A. Liddle, *Nat. Commun.* **2018**, *9*, 1715.
[49] K. B. Beckman, B. N. Ames, *Physiol. Rev.* **1998**, *78*, 547.
[50] C. Selman, T. Grune, A. Stolzing, M. Jakstadt, J. S. McLaren, J. R. Speakman, *Free Radical Bio. Med.* **2002**, *33*, 259.
[51] L. J. Mah, A. El-Osta, T. C. Karagiannis, *Leukemia* **2010**, *24*, 679.
[52] S. Sethe, A. Scutt, A. Stolzing, *Ageing Res. Rev.* **2006**, *5*, 91 .
[53] I. Bellantuono, A. Aldahmash, M. Kassem, *Bba-Mol. Basis. Dis.* **2009**, *364*, 1792.
[54] B. S. Garrison, D. J. Rossi, *Cell Metab.* **2012**, *15*, 2.
[55] Y. Haraoka, Y. Akieda, Y. Nagai, C. Mogi, T. Ishitani, *Nat. Commun.* **2022**, *13*, 1417.
[56] T. Liu, B. Xiao, F. Xiang, J. Tan, Z. Chen, X. Zhang, C. Wu, Z. Mao, G. Luo, X. Chen, J. Deng, *Nat. Commun.* **2020**, *11*, 2788 .
[57] W. N. Arifin, W. M. Zahiruddin, *Malays J. Med. Sci.* **2017**, *101*, eabi7282.
[58] Y. Liu, G. Dzidotor, T. T. Le, T. Vinikoor, K. Morgan, E. J. Curry, R. Das, A. McClinton, E. Eisenberg, L. N. Apuzzo, K. T. M. Tran, P. Prasad, T. J. Flanagan, S.-W. Lee, H. o.-M. Kan, M. T. Chorsi, K. W. H. Lo, C. T. Laurencin, T. D. Nguyen, *Sci. Transl. Med.* **2022**, *14*, eabi7282.

© 2024 Wiley-VCH GmbH

16163028, 0, Downloaded from https://onlinelibrary.wiley.com/doi/10.1002/adfm.202410931 by Cas-Beijing Institution Of, Wiley Online Library on [05/09/2024]. See the Terms and Conditions (https://onlinelibrary.wiley.com/terms-and-conditions) on Wiley Online Library for rules of use; OA articles are governed by the applicable Creative Commons License